Bidirectional Power Balance Control of Serial Voltage Injection Converter for Impedance Measurement of Grid-Connected Inverter

Junpeng Ma, *Member, IEEE*, Weitao Wang, Shunliang Wang, *Member, IEEE*,
Tianqi Liu, *Senior Member, IEEE*, and Jingbo Zhao

***Abstract*—Serial voltage injection (SVI) converter is widely used in frequency-scan for the impedance measurement of the grid-connected inverter. The dc power supply is necessary for the SVI converter, which reduces device power density and cost performance. Meanwhile, the fundamental voltage variation brought by the varying operating capacity of the inverter and the voltage drop on the grid impedance decreases the impedance measurement precision in the traditional control scheme. In this article, the bidirectional power balance control strategy is first proposed to maintain the dc voltage without an additional dc power supply. Then, a voltage reference calculation method is proposed for regulating fundamental voltage. By the proposed method, the SVI converter can inject broadband-frequency voltage perturbations into the system under test with constant dc-side voltage and desired ac-side voltage. The impedance accuracy is not affected by the operating capacity of the inverter and the impedance of the grid with the proposed control method. The proposed power balance control with fundamental voltage control of the SVI converter is verified by the experimental tests.**

***Index Terms*—Bidirectional power control, fundamental voltage control, impedance measurement, serial voltage perturbation injection.**

I. INTRODUCTION

WITH the increasing penetration of renewable energy, e.g., wind/photovoltaic power generation in power systems, power electronics converters are being commonly utilized as the interface between renewable energy power generation systems and the grid. The interactions between the converter and the grid have led to small-signal instability due to their highly nonlinear behavior [1]. Hence, it is essential to analyze the small-signal instability, which is usually manifested as the broadband oscillatory phenomenon occurring in the grid-connected inverter and the grid. There are mainly two types of methods to analyze the stability of renewable energy integrated power systems: the root-locus-based [2] as well as other time-domain analytical methods, and the impedance-based methods [3]. The root-locus-based method needs to solve high-order characteristic equations of the system, which is also difficult to analyze the eigenvalue. Currently, the impedance-based method is usually applied for stability analysis. The ratio of the grid impedance to the inverter input impedance is an effective stability criterion. The equivalent impedance of the grid-connected inverter can be derived by modeling or measurement [4], [5], [6], [7]. However, accurate controller parameters are required in the analytical impedance modeling of the inverter. These detailed parameters are usually difficult to obtain from the encapsulated product. In contrast, the inverter is regarded as a black-box model and the equivalent input impedance of this black box can be acquired by measurement, which does not require the detailed parameters of the inverter. Therefore, impedance measurement is a promising method in impedance-based stability analysis.

Impedance measurement methods can be divided into noninvasive measurement methods and invasive measurement methods [8]. Noninvasive measurement method uses the existing harmonics in the system, such as load switching, the background harmonics of the system, etc., to get the impedance information at a specific frequency. This method does not require any excitation sources. In [9], the switching capacitor method generates harmonic signals by changing the switching state of the capacitor in the power system, but the disturbance current amplitude cannot be controlled.

The invasive measurement method usually can measure more accurate impedance information, which uses impedance measurement units (IMUs) to inject desired perturbations into the system under test, and the inverter input impedance is derived by analyzing the response with the desired injections with Discrete Fourier Transform. There are many different IMUs generating perturbations for impedance measurement. Liu et al. [10] injected current perturbation into the system by using a power amplifier. The harmonic current is injected into the system by using a chopper circuit composed of resistors connected

---

Manuscript received 22 June 2022; revised 30 September 2022, 26 November 2022, and 16 January 2023; accepted 13 March 2023. Date of publication 21 March 2023; date of current version 20 April 2023. This work was supported by the National Natural Science Foundation of China under Grant 52207216. Recommended for publication by Associate Editor M. Molinas. *(Corresponding author: Shunliang Wang.)*

Junpeng Ma, Shunliang Wang, and Tianqi Liu are with the College of Electric Engineering and Information Technology, Sichuan University, Chengdu 610065, China (e-mail: junpeng_ma@163.com; slw_scu@163.com; tqliu@scu.edu.cn).

Weitao Wang is with the College of Electrical Engineering, Sichuan University, Chengdu 610065, China (e-mail: fredwwt@163.com).

Jingbo Zhao is with the Power Science Research Institute of State Grid Jiangsu Electric Power Company, Ltd., Nanjing 210024, China (e-mail: zhaojb1@js.sgcc.com.cn).

Color versions of one or more figures in this article are available at https://doi.org/10.1109/TPEL.2023.3258632.

Digital Object Identifier 10.1109/TPEL.2023.3258632

in series with transistors in [11]. The above two mentioned solutions both have limitations in high-impedance measurement. A voltage amplifier, which injects the perturbation current into the system under test, is discussed in [12]. Yet, it can only measure the impedance at low-voltage power systems up to 100 kW. Further, a three-phase low switching frequency chopper circuit for current perturbation injection is presented in [13], and the injection current contains considerable harmonics by using this topology. In [14], the three-phase bridge converter is applied for current injection with relatively low frequencies.

The IMU with shunt current injection solution is mainly used for the measurement of the low impedance, while the serial voltage injection (SVI) can measure high impedance more accurately [15]. Sumner et al. [16] injected transient voltage perturbation into the network under test by an ideal controlled voltage source. The interleaved power electronics building blocks are used in [17] for the SVI with the additional dc power supply. In [18], the interleaved H-bridge modules are used to inject voltage perturbation. However, the impedance measurement accuracy of the SVI method is remarkably affected by the potential variation of the fundamental voltage at the point of common coupling (PCC), which is brought by the grid impedance and operating capacity of the system under test [19], [20], [21].

The IMU, dynamic voltage restorer (DVR), active power filter (APF), and static synchronous compensator (STATCOM) in the high-power system are widely utilized in fundamental voltage compensation, harmonic rejection, and reactive power compensation. DVR is used to compensate for the fundamental voltage sag/swell to maintain the equilibrium point of the load but requires an extra dc power supply [22], [23], [24], [25]. APF and STATCOM are applied in harmonic filtration [26], [27], [28], [29] and reactive power compensation [30], [31], [32], [33], respectively. Yet, APF and STATCOM lack the ability of voltage perturbation injection. The existing IMU with the SVI strategy [17] also requires an extra dc supply and cannot regulate the voltage at PCC. At present, the high power density IMU with the ability to regulate fundamental voltage is not proposed yet.

To accurately measure the input impedance of the grid-connected inverter in different operating conditions, this article proposes a control scheme for the IMU using an H-bridge converter. Compared to existing IMUs, the proposed SVI converter for the IMU does not require an additional dc power supply to support dc-bus voltage, which increases the power density and cost performance. The proposed control strategy is designed to regulate the voltage amplitude at PCC to the desired voltage, which corresponds to the condition of different grid impedances and operating capacities, while a range of 5–1000 Hz serial voltage is injected into the system under test. And the impedance measurement accuracy is thereby not affected by the operating capacity of the inverter and the impedance of the weak grid.

The rest of this article is organized as follows: Section II describes the structure of the SVI converter and the grid-connected inverter. The mathematical model of the SVI converter is established in the s-domain and the output impedance model of the inverter is introduced. In Section III, the power distribution is analyzed first, and the bidirectional voltage balance control and the fundamental voltage control are proposed for the SVI converter. In Section IV, a semi-physical simulation verification is carried out to verify the effectiveness of the proposed control scheme for a grid-connected inverter of 5 kW. In Section V, the proposed control method is verified in the scaled-down experimental platform of 330 W. Section VI concludes this article.

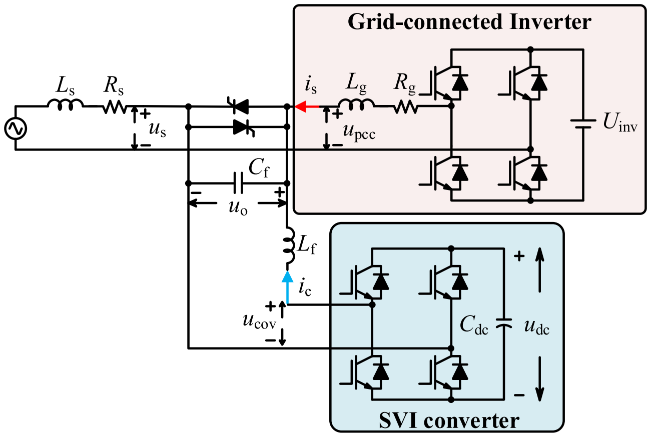

Fig. 1. SVI converter and the grid-connected inverter.

II. SYSTEM DESCRIPTION AND MATHEMATICAL MODEL

A. *System Description and the Mathematical Model*

Fig. 1 depicts the topology of the SVI converter using one H-bridge module, and the grid-connected inverter with an L-filter, where L_s and R_s represent the grid Thevenin impedance. L_g and R_g represent the filter inductance and its equivalent resistance of the inverter, respectively. And R_s, R_g usually can be neglected. u_s is the grid voltage. u_{pcc} is the voltage at PCC. i_s is the grid-side current of the inverter. U_{inv} is the dc-side voltage of the inverter. u_o is the output voltage of the SVI converter. i_c is the output current of the SVI converter. L_f and C_f represent the filter capacitance and inductance of the SVI converter, respectively. C_{dc} is the dc-side capacitance of the H-bridge converter. u_{cov} is the output voltage of the H-bridge converter and u_{dc} is the voltage across C_{dc}. The bidirectional thyristor is used to isolate the SVI converter from the grid inverter before measurement. At the initial instant of impedance measurement, the bidirectional thyristor will be switched OFF for connecting the SVI converter to the PCC in series.

According to Fig. 1, the mathematical model of the measuring system can be established as

$$\begin{cases} u_s + u_o = u_{\text{pcc}} \\ C_f \frac{\mathrm{d}u_o}{\mathrm{d}t} = i_s + i_c \\ L_f \frac{\mathrm{d}i_c}{\mathrm{d}t} = u_{\text{cov}} - u_o \end{cases} \tag{1}$$

and the block diagram of the measurement system in the s-domain is shown in Fig. 2, in which the SVI converter can be analyzed as a basic second-order system.

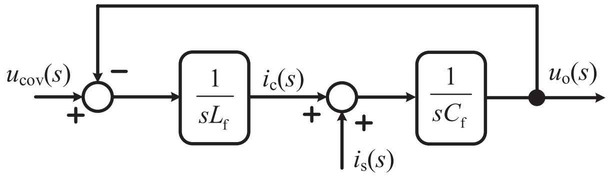

Fig. 2. Block diagram of the measurement system.

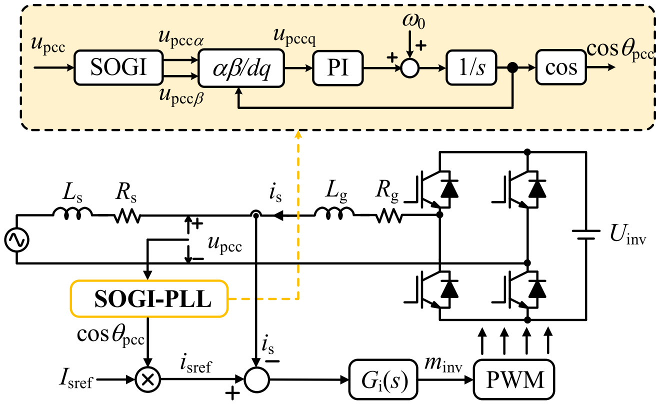

Fig. 3. Control loop of the grid-connected inverter.

B. Impedance Model of the Grid-Connected Inverter

The single-phase grid-connected inverter is usually controlled as a current source in the unit power factor [34]. And the control loop is shown in Fig. 3, where the proportional-resonant (PR) controller is used to track the sinusoidal reference i_{sref} accurately and the phase-locked loop based on second-order generalized integral (SOGI-PLL) [35] is used to provide the phase θ_{pcc} of the voltage at PCC, and m_{inv} is the modulation wave of the inverter.

Based on the Thevenin theorem, the output impedance of the inverter $Z_{inv}^{(s)}$ can be derived from the current control loop shown in Fig. 3. The transfer function of $Z_{inv}^{(s)}$ is expressed as

$$Z_{inv}^{(s)} = \frac{u_{pcc}(s)}{i_s(s)} = \frac{sL_g + R_g + G_i(s)e^{-1.5Ts}}{G_{PLL}^{(s)} G_i(s)e^{-1.5Ts} - 1} \tag{2}$$

where $G_i^{(s)}$ is the transfer function of the PR controller and T is the sampling period. $G_{PLL}^{(s)}$ is the transfer function from u_{pcc} to the current reference i_{sref} [36], which is expressed as

$$\begin{cases} G_{PLL}^{(s)} = \frac{I_{sref}}{2}[T_{pll}(s - j\omega_0) + T_{pll}(s + j\omega_0)]d(s) \\ +j\frac{I_{sref}}{2}[T_{pll}(s - j\omega_0) - T_{pll}(s + j\omega_0)]q(s) \\ T_{pll}^{(s)} = \frac{G_{PI-PLL}^{(s)}}{s + u_{pcc}G_{PI-PLL}^{(s)}} = \frac{K_{P-PLL}s + K_{I-PLL}}{s^2 + u_{pcc}(K_{P-PLL}s + K_{I-PLL})} \end{cases} \tag{3}$$

where $d(s)$ and $q(s)$ are the transfer functions of SOGI, which are used to construct the orthometric components. ω_0 is the fundamental frequency of the grid and $G_{PI-PLL}^{(s)}$ is the transfer function of the PI controller for SOGI-PLL. From (3), it can be seen that $G_{PLL}^{(s)}$ is affected by I_{sref} and u_{pcc} especially when u_{pcc} is relatively low and the operating capacity of the inverter is high.

TABLE I
PARAMETERS OF THE GRID-CONNECTED INVERTER

Parameter	Value
L_g	2 mH
K_p, K_r	10, 6000
$K_{P\text{-}PLL}$, $K_{I\text{-}PLL}$	1, 99
u_{pcc}	311 V
I_{sref}	32 A
Switching frequency	10 kHz

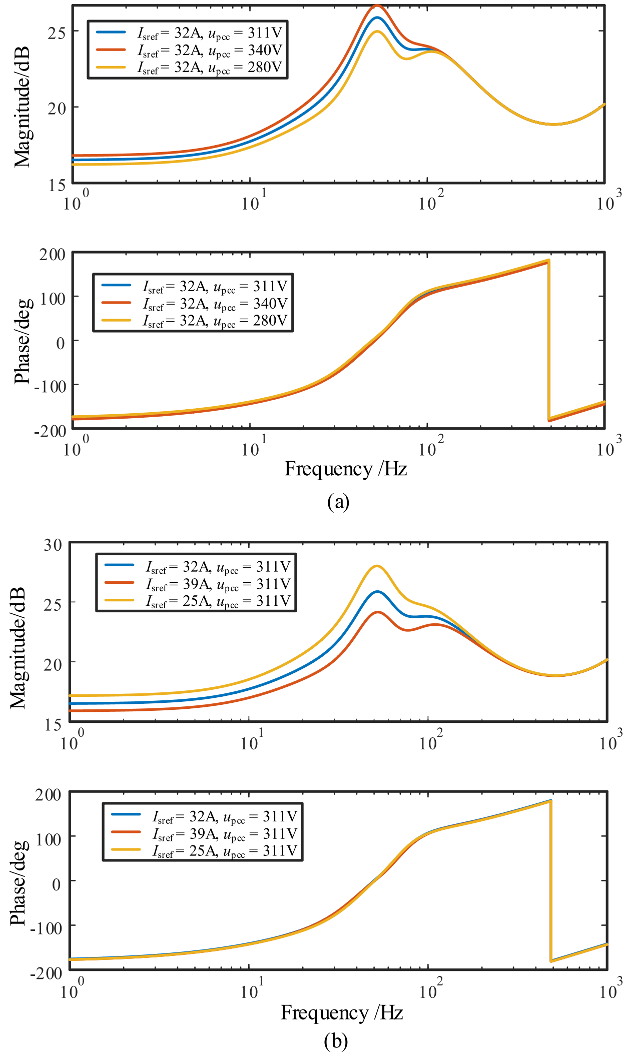

Fig. 4. Frequency response of $Z_{inv}^{(s)}$ when u_{pcc} and I_{sref} are different.

Consequently, $Z_{inv}^{(s)}$ derived from Fig. 3 and Table I will be changed with the fundamental voltage variation and current reference variation of the inverter, as shown in Fig. 4.

III. CONTROL STRATEGY OF THE SVI CONVERTER

A. Bidirectional Power Balance Control

The stable dc bus voltage is essential for the SVI converter to inject perturbation. Therefore, the bidirectional power balance control is proposed to regulate the dc capacitor voltage.

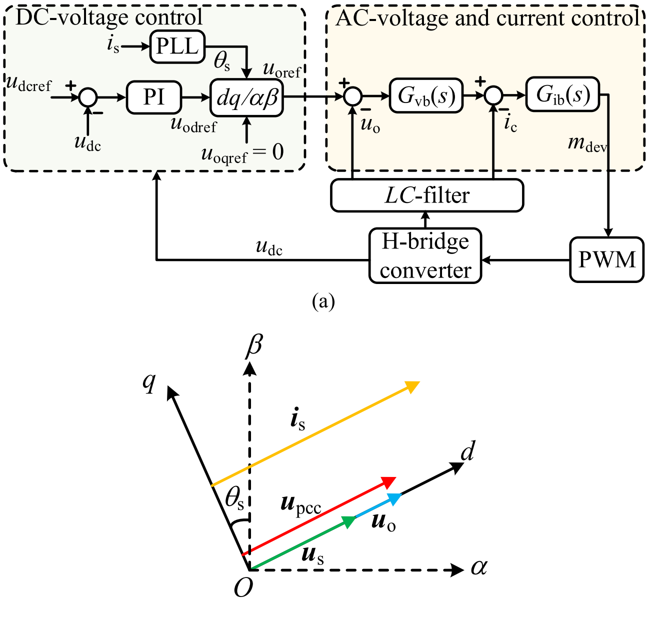

(a)

(b)

Fig. 5. Operation principles of bidirectional power balance control. (a) Block diagram of bidirectional power balance control. (b) Vector diagram of $\boldsymbol{u}_o$, $\boldsymbol{i}_s$, $\boldsymbol{u}_s$, and $\boldsymbol{u}_{\text{pcc}}$.

Converter loss, e.g., switching loss and loss of dc side equivalent resistor leads to the decrease of dc voltage. The SVI converter should absorb active power ΔP from the grid to balance the converter loss ΔP_{loss}. In the dq rotating frame, the active power absorbed by the SVI converter can be calculated as

$$\Delta P = \frac{u_{od} i_{sd} + u_{oq} i_{sq}}{2} \tag{4}$$

where u_{od} and i_{sd} are the d-axis components of the output voltage vector $\boldsymbol{u}_o$ of SVI inverter and inverter current vector $\boldsymbol{i}_s$, respectively. u_{oq} and i_{sq} are the q-axis components of the output voltage vector $\boldsymbol{u}_o$ of the SVI inverter and inverter current vector $\boldsymbol{i}_s$, respectively.

To simplify (4), the d-axis can be set aligned by SOGI-PLL with $\boldsymbol{i}_s$, in which the q-axis component of $\boldsymbol{i}_s$ is zero. And (4) can be rewritten as

$$\Delta P = \frac{u_{od} i_{sd}}{2}. \tag{5}$$

It is obvious that ΔP can be controlled by regulating the value of u_{od} considering i_{sd} as constant. Fig. 5(a) shows the block diagram of the bidirectional power balance control, where u_{dcref} is the dc bus voltage reference. u_{dc} is the dc voltage of the H-bridge converter. $u_{od\text{ref}}$ and $u_{oq\text{ref}}$ represent the d-axis and q-axis references of the output voltage vector $\boldsymbol{u}_o$, respectively. θ_s is the phase angle of $\boldsymbol{i}_s$. $u_{o\text{ref}}$ is the α-axis reference of $\boldsymbol{u}_o$ in the $\alpha\beta$ stationary frame. m_{dev} is the modulation voltage.

In bidirectional power balance control, the active power ΔP is reflected by the difference between u_{dcref} and u_{dc}. $u_{od\text{ref}}$ is calculated by the PI controller to regulate ΔP as demand in terms of (5). As shown in Fig. 5(a), $G_{\text{vb}}^{(s)}$ and $G_{\text{ib}}^{(s)}$ represent the transfer functions of voltage-outer-loop PR controller and current-inner-loop PR controller, which are used to track $u_{o\text{ref}}$ in stationary frame rapidly and accurately.

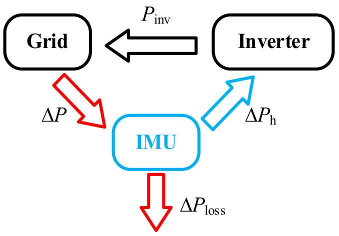

Fig. 6. Power flow among the SVI converter and system under test.

Furthermore, $\boldsymbol{u}_o$ is controlled to be aligned with $\boldsymbol{i}_s$ in the steady state. And $\boldsymbol{i}_s$ is aligned with $\boldsymbol{u}_{\text{pcc}}$ in the condition of the unit power factor [34]. According to (1), the vector diagram of $\boldsymbol{u}_o$, $\boldsymbol{i}_s$, $\boldsymbol{u}_s$, and $\boldsymbol{u}_{\text{pcc}}$ in stationary and rotating frames can be derived as shown in Fig. 5(b). It is clear that the amplitude of $\boldsymbol{u}_{\text{pcc}}$ will be greater than $\boldsymbol{u}_s$ due to the existence of $\boldsymbol{u}_o$, which is regulated to absorb active power for the SVI converter for balancing the active power between the grid side and the dc side of the H-bridge converter.

B. Voltage Perturbation Injection and Power Flow Analysis

The variation of $\boldsymbol{u}_{\text{pcc}}$ under bidirectional power balance control is very little due to the slight loss of the H-bridge converter. However, the variation of $\boldsymbol{u}_{\text{pcc}}$ could be greater when perturbation voltage is injected into the system under test. From the aspect of power flow shown in Fig. 6, the power flow among the SVI converter and the system under test includes four parts: P_{inv} generated by the inverter, ΔP, ΔP_{loss}, and the perturbation power ΔP_h. In the voltage perturbation injection process, ΔP_h absorbed by the inverter's equivalent impedance is completely provided by the SVI converter; ΔP is absorbed by SVI converter to balance ΔP_{loss} and ΔP_{h} to support the dc voltage. According to Figs. 1 and 6 and (5), the relationship of power flow between the SVI converter and the system under test satisfies

$$\begin{cases} \Delta P = \Delta P_h + \Delta P_{\text{loss}} = \frac{u_{od} i_{sd}}{2} \\ \Delta P_h = \frac{1}{2} u_{\text{pcc}h} i_{sh} \cos\theta_h = \frac{u_{oh}^2 \cos[\angle Z_{\text{inv}}^{(\text{j}\omega_{\text{h}})}]}{2\left|Z_{\text{inv}}^{(\text{j}\omega_{\text{h}})}\right|} \end{cases} \tag{6}$$

where $u_{\text{pcc}h}$, i_{sh}, and u_{oh} are the injected harmonic components of u_{pcc}, i_s, and u_o, respectively; θ_h is the phase difference of $u_{\text{pcc}h}$ and i_{sh}; and ω_h is the injected harmonic frequency. From (6), it can be concluded that ΔP_h will be larger if $|Z_{\text{inv}}^{(j\omega_h)}|$ is small at some perturbation frequencies, and u_{od} and u_{pcc} will thereby remarkably vary.

Fig. 7 shows the control block diagram of voltage perturbation injection, where $u_{oh\text{ref}}$ is the injection perturbation voltage reference from 5 to 1000 Hz; $G_{vh}^{(s)}$ and $G_{ih}^{(s)}$ represent the transfer functions of PR controllers for the perturbation voltage and current, respectively.

It can be illustrated from Fig. 7 that the perturbation voltage and current controllers are connected with the bidirectional power balance controller in parallel to construct the multiple

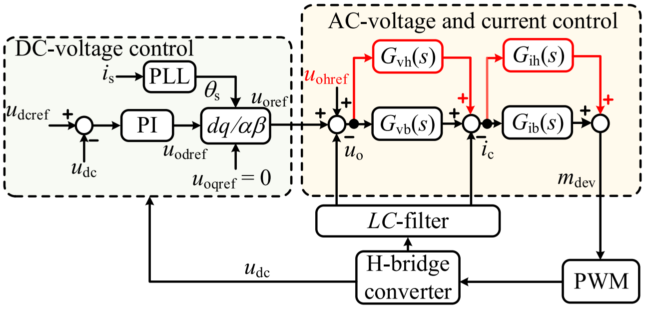

Fig. 7. Block diagram of voltage perturbation injection.

PR controllers (MPR) [37], which are utilized for tracking fundamental and harmonic components and avoiding the harmonics interaction with each other. Therefore, the proposed method offers two isolated control paths for the SVI converter to achieve the active power balance in the fundamental-frequency domain and the voltage perturbation injection in the harmonic-frequency domain simultaneously. The parameter design for the MPR controller can be referred to in [18].

C. Fundamental Voltage Control

In the weak grid, which means the equivalent impedance of the grid is quite large, the fundamental component of u_{pcc} can be calculated as

$$u_{\text{pcc}}^{(\text{j}\omega_0)} = u_s + (\text{j}\omega_0 L_s + R_s) i_s(\text{j}\omega_0). \tag{7}$$

Apparently, u_{pcc} will change remarkably under different power ratings P_{inv} since the voltage drop of the impedance of the grid is too large to be neglected.

From (3), the output impedance of the inverter is affected by the fundamental amplitude of $\boldsymbol{u}_{\text{pcc}}$. It is inevitable that $\boldsymbol{u}_{\text{pcc}}$ will change under perturbation injection and vary widely due to the large impedance of the weak grid. Thus, the fundamental amplitude of $\boldsymbol{u}_{\text{pcc}}$ should be regulated to the rated value to suppress the influence of the grid impedance and the perturbation injection on PCC voltage. Furthermore, the amplitude of $\boldsymbol{u}_{\text{pcc}}$ is also supposed to be controlled to any desired values including the rated value to simulate the different equilibrium points for the complicated grid conditions.

It is assumed that the voltage vector $\boldsymbol{u}_{\text{pcc}}$ and the current vector $\boldsymbol{i}_s$ are oriented to d-axis. In the dq rotating frame with the fundamental frequency, the vectors $\boldsymbol{u}_o$, $\boldsymbol{i}_s$, $\boldsymbol{u}_s$, and $\boldsymbol{u}_{\text{pcc}}$ should satisfy

$$\begin{cases} u_{od} i_{sd} = 2\Delta P \\ u_{sd} + u_{od} = u_{\text{pcc}d} \\ u_{sq} + u_{oq} = u_{\text{pcc}q} \\ u_{\text{pcc}d}^2 + u_{\text{pcc}q}^2 = \left(u_{\text{pcc}}^{\text{ref}}\right)^2 \end{cases} \tag{8}$$

where u_{sd} and $u_{\text{pcc}\,d}$ are the d-axis components of the vectors $\boldsymbol{u}_s$ and $\boldsymbol{u}_{\text{pcc}}$, respectively. u_{sq} and $u_{\text{pcc}\,q}$ are the q-axis components of the vectors $\boldsymbol{u}_s$ and $\boldsymbol{u}_{\text{pcc}}$, respectively. $u_{\text{pcc}}^{\text{ref}}$ is the desired fundamental amplitude of $\boldsymbol{u}_{\text{pcc}}$ corresponding to the conditions of different grid impedances and operating capacities.

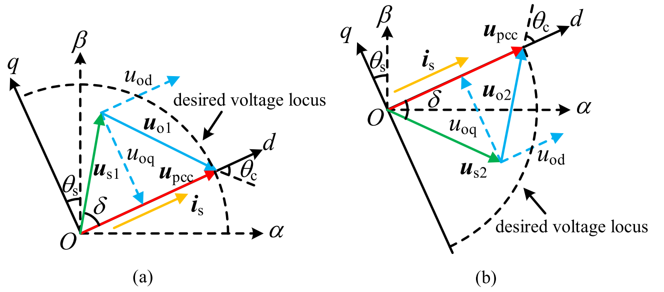

Fig. 8. Vector diagram of $\boldsymbol{u}_o, \boldsymbol{i}_s, \boldsymbol{u}_s$, and $\boldsymbol{u}_{\text{pcc}}$ in voltage compensation mode.

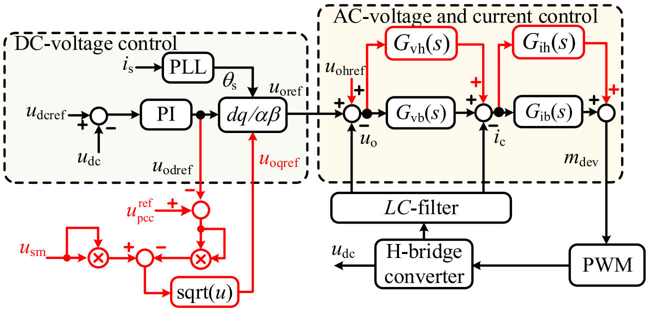

Fig. 9. Block diagram of fundamental voltage control.

Fig. 8 shows the vector diagram in stationary and rotating frames. $\boldsymbol{u}_{o1}$ and $\boldsymbol{u}_{o2}$ are the two possible solutions for the output voltage vector $\boldsymbol{u}_o$. Correspondingly, $\boldsymbol{u}_{s1}$ and $\boldsymbol{u}_{s2}$ are the two possible vectors for $\boldsymbol{u}_s$; θ_c is the phase difference between $\boldsymbol{u}_{o1}(\boldsymbol{u}_{o2})$ and $\boldsymbol{i}_s$. The radius of the desired voltage locus is equal to $u_{\text{pcc}}^{\text{ref}}$.

It is noted that the vector $\boldsymbol{u}_s$ is possibly not constrained on the desired voltage locus due to the existence of grid impedance. Yet, the end of the vector $\boldsymbol{u}_{\text{pcc}}$ should be controlled to travel on the locus.

From the geometry and relationships of the vectors, the voltage reference can be calculated in the dq rotating frame. It is clear that ΔP can be characterized by u_{odref} according to (5). In terms of u_{odref} calculated from bidirectional power balance control, the q-axis reference u_{oqref} and the generated reactive power ΔQ can be derived from (8) and Fig. 8 as

$$\begin{cases} u_{oqref} = \pm\sqrt{u_{sm}^2 - \left(u_{\text{pcc}}^{\text{ref}} - u_{odref}\right)^2} \\ \Delta Q = \frac{u_{oq} i_{sd}}{2} \end{cases} \tag{9}$$

where u_{sm} is the amplitude of $\boldsymbol{u}_s$.

Fig. 9 shows the block diagram of fundamental voltage control using the positive solution of $u_{oq\text{ref}}$. Apparently, the existence of θ_c induces the reactive power interaction between the SVI converter and the grid, which is used to regulate the amplitude of $\boldsymbol{u}_{\text{pcc}}$. And there are also two solutions of $u_{oq\text{ref}}$ according to (9), both of which can be applied in the fundamental voltage control and determine the types of reactive power generated by the SVI converter. Moreover, u_{oqref} can be adjusted automatically as ΔP changes, and voltage vectors thereby are constrained in the designed voltage locus without considering the grid impedance.

TABLE II
PARAMETERS OF THE SYSTEM UNDER TEST OF 5 KW AND THE GRID

Parameter	Value
L_{s}	1 mH
L_{g}	2 mH
U_{inv}	380 V
Switching frequency	10 kHz
Rated value of voltage at PCC u_{pcc}	311 V (1 p.u.)
Rated value of system current i_{s}	32 A (1 p.u.)

TABLE III
PARAMETERS OF THE SVI CONVERTER

Parameter	Value
C_{f}	100 μF
L_{f}	100 μH
C_{dc}	3000 μF
Switching frequency	10 kHz
Rated value of u_{dc}	200 V (1 p.u.)
Rated value of u_{o}	31 V

D. Control Process of the SVI Converter

To inject voltage perturbation into the system under test successfully, four steps are designed in the SVI procedure.

1) Precharge: SVI converter is first connected in parallel with the grid voltage. The SVI converter is blocked, and the grid voltage charges the capacitor of the H-bridge by uncontrolled rectifier mode. Then, the bidirectional thyristor is switched ON to bypass the SVI converter from the system. And then the SVI converter and grid-connected inverter are connected as Fig. 1.

2) Bidirectional Power Balance Control: The bidirectional thyristor is switched OFF and the main circuit of the SVI converter is connected to the system. Then, the bidirectional power balance control is enabled. The q-axis reference $u_{oq\mathrm{ref}}$ is set as zero, and the dc-voltage controller, the grid voltage, and current controllers are used for regulating the dc voltage to the rated value.

3) Fundamental Voltage Control: After the dc-side voltage is stable, the q-axis reference is calculated in terms of (9) and the reference $u_{o\mathrm{ref}}$ is updated in real time.

4) Voltage Perturbation Injection: After the fundamental voltage control, the perturbation voltage reference $u_{oh\mathrm{ref}}$ is given with the specific frequency in the range of 5–1000 Hz. And the resonant frequency of MPR controllers is the same as that of $u_{oh\mathrm{ref}}$. After measuring the output current response of the grid-connected inverter at the specific frequency, the given perturbation frequency is changed and repeat the above steps.

IV. SIMULATION TEST

The semi-physical simulation tests are executed to verify the effectiveness of the control strategy for the SVI converter proposed in this article. The tests include the fundamental voltage control strategy verification and output impedance measurement of the grid-connected inverter and comparisons of the traditional method and the traditional SVI method [18] are given. The semi-physical test platform consists of the simulator RT-BOX, which is applied to simulate the main circuit of the SVI converter and grid-connected inverter, the digital signal processor TMS320F28379 used as the controller to realize the proposed control strategy.

The detailed parameters are given in Tables II and III, where the parameters are specifically designed for an equivalent renewable energy generation system of 5 kW and the SVI converter. The grid impedance L_s is designed for 10% fundamental voltage drop at PCC [38], the L_g of L-filter is designed for suppressing the current ripple, which is smaller than 10% fundamental component of i_s [39], and the cutoff frequency of the LC-filter (L_f, C_f) is designed to be higher than 1000 Hz, which is the maximum frequency of the perturbation injected by the SVI converter. The capacitance of the dc-side capacitor applied in the SVI converter (C_{dc}) is designed for 1% voltage ripple in dc side [40].

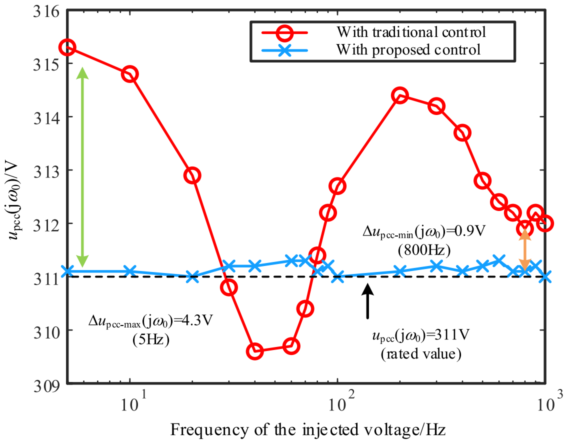

Fig. 10. Variation of $u_{\mathrm{pcc}}^{(jw_0)}$ in a stiff grid during voltage perturbation injection.

Fig. 10 shows the variation of $u_{\mathrm{pcc}}^{(jw_0)}$ in the stiff grid. When the fundamental voltage control is disabled, it can be seen that $u_{\mathrm{pcc}}^{(jw_0)}$ changes with the injected voltage frequency and $u_{\mathrm{pcc}}^{(jw_0)}$ exhibits considerable variation with the traditional method, which is in consistent with the analytical curve of $|Z_{\mathrm{inv}}(s)|$ shown in Fig. 4. In contrast, $u_{\mathrm{pcc}}^{(jw_0)}$ remains around the rated value of 311 V with the proposed method. The maximum variation of $u_{\mathrm{pcc}}^{(jw_0)}$ is 4.3 V with a perturbation of 5 Hz and the minimum variation of $u_{\mathrm{pcc}}^{(jw_0)}$ is 0.9 V with a perturbation of 800 Hz.

Fig. 11 shows the variation of $u_{\mathrm{pcc}}^{(jw_0)}$ in a weak grid, where L_s is 10 mH during the perturbation injection process. The maximum variation of $u_{\mathrm{pcc}}^{(jw_0)}$ is 43.94 V with the perturbation of 40 Hz, 8 kW, and the minimum variation of $u_{\mathrm{pcc}}^{(jw_0)}$ is 0.3 V with the perturbation of 300 Hz, 3 kW with the traditional method. $u_{\mathrm{pcc}}^{(jw_0)}$ remains the rated value of 311 V with the proposed method. It is clear that $u_{\mathrm{pcc}}^{(jw_0)}$ changes more remarkably in the weak grid according to Figs. 10 and 11.

Fig. 12 illustrates that the proposed method can control the fundamental voltage at PCC to the desired voltage (e.g., 80% and 90% of the rated voltage at PCC) to simulate different values of $u_{\mathrm{pcc}}^{(jw_0)}$ under variable grid conditions.

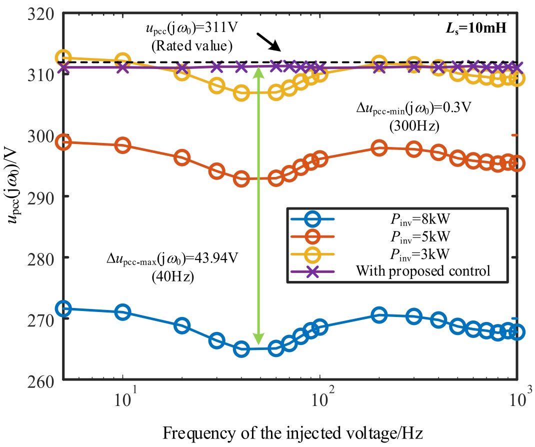

Fig. 11. Variation of $u_{\mathrm{pcc}}^{(jw_0)}$ in a weak grid during voltage perturbation injection.

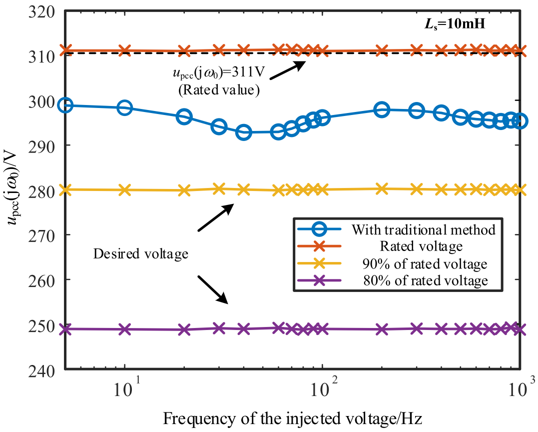

Fig. 12. Proposed fundamental voltage control method for the desired voltage.

Fig. 13 shows the simulation test of the output admittance measurement of the inverter in the weak grid. From Fig. 12, it is clear that the amplitude of $Y_{\mathrm{inv}}^{(s)}$ with the traditional control scheme exists the deviation mainly at 20–80 Hz, in which the magnitude measurement errors are 3.2%, 4.3%, 4.4%, 5.0%, and 3.6%, respectively. The impedance measurement errors are mainly brought by the larger fundamental voltage variation in the weak grid.

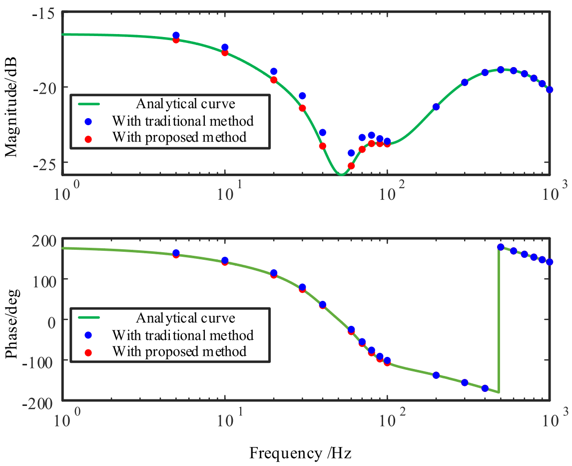

Fig. 13. Output admittance $Y_{\mathrm{inv}}^{(s)}$ measurement test for the inverter of 5 kW in a weak grid.

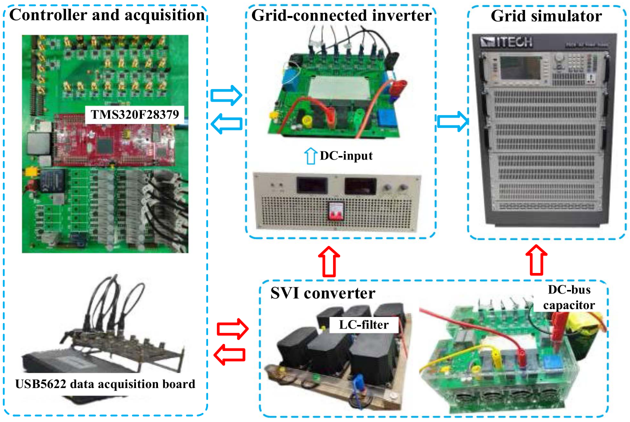

Fig. 14. Experimental platform for inverter of 330 W and SVI converter.

TABLE IV
EXPERIMENTAL PARAMETERS OF THE SYSTEM UNDER TEST OF 330 W

Parameter	Value
L_g	2 mH
U_{inv}	220 V
Switching frequency	10 kHz
Rated value of u_{pcc} (rms)	110 V
Rated value of i_s (rms)	3 A
IGBT module	1200 V, 25 A

V. EXPERIMENTAL TEST

The experimental platform shown as Fig. 14 is used for the frequency-scan test for a grid-connected inverter of 330 W, and ITECH ac power supply is applied to simulate a stiff grid. The inverter and SVI converter are managed by a TMS320F28379 digital signal processor. The data acquisition board USB5622 is applied to acquire the waveform data of u_{pcc}, i_s, and the waveform data will be uploaded to the host computer for impedance calculation and analysis. The effectiveness of the proposed control scheme is verified by frequency-scan test for grid-connected inverter. The detailed system parameters for the scaled-down experimental test including the system under test of 330 W and the SVI converters are shown in Tables IV and V.

In the experimental test, the rated current of the inductors applied in the inverter (L_g) and the SVI converter (L_f) is 15 A, the rated voltage of L_g and L_f is 1000 V, and the linearity of the inductors is 90% in range of 0–15 A; the film capacitor of ANWO CLA series is applied in LC filter of the SVI converter, the rated voltage is 800 V (dc), and the tolerance is ±5%; and the electrolytic capacitor of RMHCG FA series is applied in dc side of the SVI converter, the rated voltage is 450 V (dc), and the maximum working temperature is 105 °C. The IGBT modules

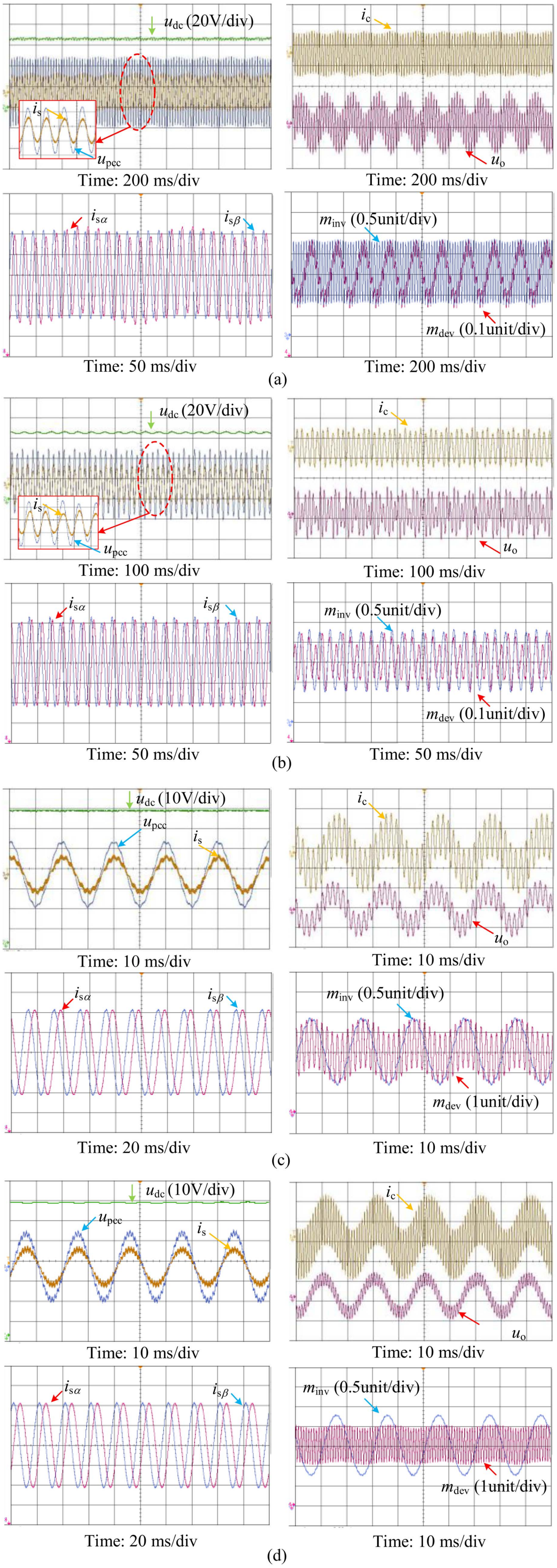

Fig. 15. Experimental waveforms of voltage perturbation injection with the frequency of (a) 5 Hz, (b) 70 Hz, (c) 500 Hz, and (d) 1000 Hz. ($u_{\rm pcc}$: 100 V/div, i_s, i_c: 5 A/div, u_o: 20 V/div, $i_{s\alpha}$, $i_{s\beta}$: 2 A/div).

TABLE V
EXPERIMENTAL PARAMETERS OF THE SVI CONVERTER

Parameter	Value
$C_{\rm f}$	20 μF
$L_{\rm f}$	1 mH
$C_{\rm dc}$	3300 μF
Switching frequency	10 kHz
Rated voltage at PCC (rms)	110 V
Rated value of $u_{\rm dc}$	65 V
Rated value of $u_{\rm o}$	10 V
IGBT module	1200 V, 25 A

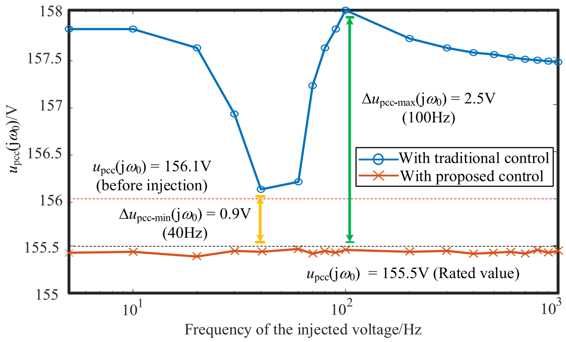

Fig. 16. Variation of $u_{\rm pcc}^{(jw_0)}$ during voltage perturbation injection.

of Infineon FS25R12W1T4 are applied for the inverter and the SVI converter, the voltage tolerance is 1200 V, and the maximum collector current is 25 A.

A. *Experimental Test for the Proposed Control Method*

Fig. 15 shows the experimental test of the proposed control test verification. The harmonic injection voltage references are the sinusoidal waveforms of which the frequencies are in the range of 5 to 1000 Hz. The test waveforms of the voltage injection in 5, 70, 500, and 1000 Hz are depicted in Fig. 15, where $u_{\rm pcc}$ and i_s are the voltage at PCC and the system current of the grid-connected inverter, respectively, $u_{\rm dc}$ is the dc bus voltage of the SVI converter, u_o and i_c are the output voltage and output current of the SVI converter, respectively, $i_{s\alpha}$ and $i_{s\beta}$ are the output orthometric components of i_s generated by the SOGI-PLL of the SVI inverter, respectively, and $m_{\rm inv}$ and $m_{\rm dev}$ are the modulation waves of the grid-connected inverter and the SVI converter, respectively. It is seen that the ripples in dc voltage are increased under relatively low-frequency perturbation.

Fig. 16 shows the amplitude variation of the $u_{\rm pcc}$ with the traditional control method and the proposed control method. The maximum variation of $u_{\rm pcc}^{(jw_0)}$ is 2.5 V with a perturbation of 100 Hz and the minimum variation of $u_{\rm pcc}^{(jw_0)}$ is 0.9 V with a perturbation of 40 Hz. And the amplitude of $u_{\rm pcc}^{(jw_0)}$ remains around the designed value of 155.5 V with the proposed method. Yet, the fundamental voltage amplitude is varied obviously with the frequency variation of the injected voltage by the traditional method.

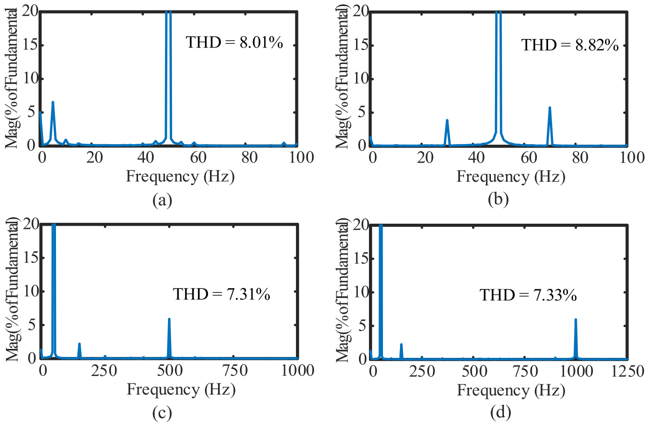

Fig. 17. THD analysis of (a) 5 Hz, (b) 70 Hz, (c) 500 Hz, and (d) 1000 Hz.

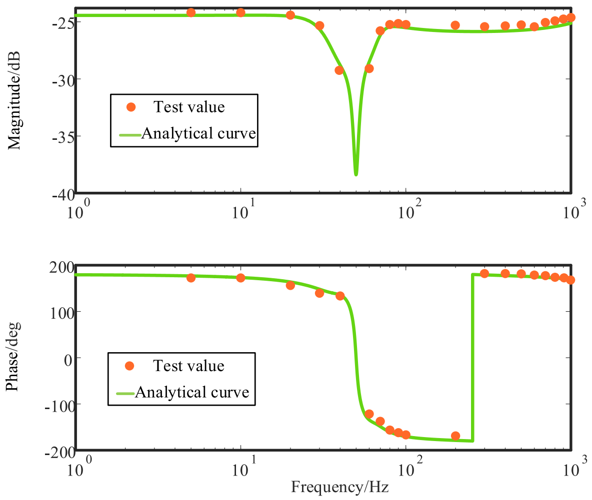

Fig. 18. Output admittance $Y_{\text{inv}}^{(s)}$ measurement test for the inverter of 330 W.

Fig. 17 shows the total harmonic distortion analysis for perturbation in range of 5, 70, 500, and 1000 Hz.

B. Impedance Measurement Test for Grid-Connected Inverter

Fig. 18 shows the experimental test of the output admittance measurement of the inverter with the proposed method. The analytical curves are drawn according to (2), and it can be seen that the experimental test values are in consistent with the analytical curves, which verifies the effectiveness of the SVI converter for the impedance measurement.

VI. CONCLUSION

In this article, a bidirectional power balance control of a single-phase SVI converter is proposed for the impedance measurement of the grid-connected inverter. The theoretical analysis of the proposed method is verified by the experimental test, and the following conclusions can be drawn as follows:

1) In the case of the injected voltage perturbation with different frequencies at a range of 5–1000 Hz, the dc voltage of the H-bridge module remains the rated value without using an additional dc supply.
2) The proposed fundamental voltage compensation scheme can control the amplitude of the voltage at PCC to any desired values for evaluating the stability of the inverter with variable operating capacities in the condition of different grid impedances.
3) The accuracy of impedance measurement is not impacted by the operating capacity of the inverter and the variable grid conditions with the proposed method.

REFERENCES

[1] H. Liu et al., “Subsynchronous interaction between direct-drive PMSG based wind farms and weak AC networks,” *IEEE Trans. Power Syst.*, vol. 32, no. 6, pp. 4708–4720, Nov. 2017.

[2] H. Wang, C. He, and L. Fu, “Stability mechanism analysis of HVDC control system for power system restoration using HVDC,” in *Proc. 4th Int. Conf. Elect. Utility Deregulation Restructuring Power Technol.*, 2011, pp. 433–437.

[3] J. Sun, “Impedance-based stability criterion for grid-connected inverters,” *IEEE Trans. Power Electron.*, vol. 26, no. 11, pp. 3075–3078, Nov. 2011.

[4] X. Wang and F. Blaabjerg, “Harmonic stability in power electronic-based power systems: Concept, modeling, and analysis,” *IEEE Trans. Smart Grid*, vol. 10, no. 3, pp. 2858–2870, May 2019.

[5] L. Harnefors, “Modeling of three-phase dynamic systems using complex transfer functions and transfer matrices,” *IEEE Trans. Ind. Electron.*, vol. 54, no. 4, pp. 2239–2248, Aug. 2007.

[6] B. Wen, D. Boroyevich, P. Mattavelli, Z. Shen, and R. Burgos, “Experimental verification of the generalized Nyquist stability criterion for balanced three-phase ac systems in the presence of constant power loads,” in *Proc. IEEE Energy Convers. Congr. Expo.*, 2012, pp. 3926–3933.

[7] X. Wang, L. Harnefors, and F. Blaabjerg, “Unified impedance model of grid-connected voltage-source converters,” *IEEE Trans. Power Electron.*, vol. 33, no. 2, pp. 1775–1787, Feb. 2018.

[8] D. Borkowski, A. Wetula, and A. Bień, “New method for noninvasive measurement of utility harmonic impedance,” in *Proc. IEEE Power Energy Soc. Gen. Meeting*, 2012, pp. 1–8.

[9] A. A. Girgis and R. B. McManis, “Frequency domain techniques for modeling distribution or transmission networks using capacitor switching induced transients,” *IEEE Trans. Power Del.*, vol. 4, no. 3, pp. 1882–1890, Jul. 1989.

[10] M. Liu, H. Yuan, Y. Sun, and C. Yang, “Research on measurement of DC power supply impedance,” in *Proc. 9th Int. Conf. Electron. Meas. Instrum.*, 2009, pp. 2–703–2–706.

[11] L. Ott, Y. Han, B. Wunder, M. Maerz, and F. Bodensteiner, “Evaluation of DC-DC-converter impedance passivity using pseudo-random test signals,” in *Proc. Int. Exhib. Conf. Power Electron. Intell. Motion Renewable Energy Energy Manage.*, 2018, pp. 1–8.

[12] G. Francis, R. Burgos, D. Boroyevich, F. Wang, and K. Karimi, “An algorithm and implementation system for measuring impedance in the D-Q domain,” in *Proc. IEEE Energy Convers. Congr. Expo.*, 2011, pp. 3221–3228.

[13] Y. A. Familiant, J. Huang, K. A. Corzine, and M. Belkhayat, “New techniques for measuring impedance characteristics of three-phase AC power systems,” *IEEE Trans. Power Electron.*, vol. 24, no. 7, pp. 1802–1810, Jul. 2009.

[14] Z. Shen, M. Jaksic, P. Mattavelli, D. Boroyevich, J. Verhulst, and M. Belkhayat, “Three-phase AC system impedance measurement unit (IMU) using chirp signal injection,” in *Proc. 28th Annu. IEEE Appl. Power Electron. Conf. Expo.*, 2013, pp. 2666–2673.

[15] Z. Xie, Y. Chen, W. Wu, and A. Luo, “A wide-bandwidth sequence-impedance online precise measurement method for renewable energy generation equipment with dual-mode disturbance,” *Proc. Chin. Soc. Elect. Eng.*, vol. 40, no. 9, pp. 2903–2914, May 2020.

[16] M. Sumner, B. Palethorpe, D. Thomas, P. Zanchetta, and M. C. Di Piazza, “Estimation of power supply harmonic impedance using a controlled voltage disturbance,” in *Proc. IEEE 32nd Annu. Power Electron. Specialists Conf.*, 2001, pp. 522–527.

[17] Z. Shen et al., “Design of a modular and scalable small-signal dq impedance measurement unit for grid applications utilizing 10 kV SiC MOSFETs,” in *Proc. 17th Eur. Conf. Power Electron. Appl.*, 2015, pp. 1–9.

[18] M. Jaksic, D. Boroyevich, R. Burgos, Z. Shen, I. Cvetkovic, and P. Mattavelli, “Modular interleaved single-phase series voltage injection converter used in small-signal dq impedance identification,” in *Proc. IEEE Energy Convers. Congr. Expo.*, 2014, pp. 3036–3045.

[19] M. Liserre, R. Teodorescu, and F. Blaabjerg, “Stability of photovoltaic and wind turbine grid-connected inverters for a large set of grid impedance values,” *IEEE Trans. Power Electron.*, vol. 21, no. 1, pp. 263–272, Jan. 2006.

[20] A. Akhavan, S. Golestan, J. C. Vasquez, and J. M. Guerrero, “Passivity enhancement of voltage-controlled inverters in grid-connected microgrids considering negative aspects of control delay and grid impedance variations,” *IEEE J. Emerg. Sel. Topics Power Electron.*, vol. 9, no. 6, pp. 6637–6649, Dec. 2021.

[21] C. Zhang, X. Wang, F. Blaabjerg, W. Wang, and C. Liu, “The influence of phase-locked loop on the stability of single-phase grid-connected inverter,” in *Proc. IEEE Energy Convers. Congr. Expo.*, 2015, pp. 4737–4744.

[22] G. A. de Almeida Carlos, C. B. Jacobina, J. P. R. A. Méllo, and E. C. Santos, “Cascaded open-end winding transformer based DVR,” *IEEE Trans. Ind. Appl.*, vol. 54, no. 2, pp. 1490–1501, Mar./Apr. 2018.

[23] P. Jayaprakash, B. Singh, D. P. Kothari, A. Chandra, and K. Al-Haddad, “Control of reduced-rating dynamic voltage restorer with a battery energy storage system,” *IEEE Trans. Ind. Appl.*, vol. 50, no. 2, pp. 1295–1303, Mar./Apr. 2014.

[24] C. Zhan et al., “Dynamic voltage restorer based on voltage-space-vector PWM control,” *IEEE Trans. Ind. Appl.*, vol. 37, no. 6, pp. 1855–1863, Nov./Dec. 2001.

[25] G. A. de Almeida Carlos, E. C. dos Santos, C. B. Jacobina, and J. P. R. A. Mello, “Dynamic voltage restorer based on three-phase inverters cascaded through an open-end winding transformer,” *IEEE Trans. Power Electron.*, vol. 31, no. 1, pp. 188–199, Jan. 2016.

[26] M. S. Hamad, M. I. Masoud, and B. W. Williams, “Medium-voltage 12-pulse converter: Output voltage harmonic compensation using a series APF,” *IEEE Trans. Ind. Electron.*, vol. 61, no. 1, pp. 43–52, Jan. 2014.

[27] S. Rahmani, N. Mendalek, and K. Al-Haddad, “Experimental design of nonlinear control technique for three-phase shunt active power filters,” *IEEE Trans. Ind. Electron.*, vol. 57, no. 10, pp. 3364–3375, Oct. 2010.

[28] S. Rahmani, A. Hamadi, and K. Al-Hadad, “A Lyapunov-function-based control for a three-phase shunt hybrid active filter,” *IEEE Trans. Ind. Electron.*, vol. 59, no. 3, pp. 1418–1429, Mar. 2012.

[29] Z. Chen, Y. Luo, and M. Chen, “Control and performance of a cascaded shunt active power filter for aircraft electric power system,” *IEEE Trans. Ind. Electron.*, vol. 59, no. 9, pp. 3614–3623, Sep. 2012.

[30] L. Wang, C.-S. Lam, and M.-C. Wong, “A hybrid-STATCOM with wide compensation range and low DC-link voltage,” *IEEE Trans. Ind. Electron.*, vol. 63, no. 6, pp. 3333–3343, Jun. 2016.

[31] B. Gultekin and M. Ermis, “Cascaded multilevel converter-based transmission STATCOM: System design methodology and development of a 12 kV ±12 MVAr power stage,” *IEEE Trans. Power Electron.*, vol. 28, no. 11, pp. 4930–4950, Nov. 2013.

[32] D. Lu, C. Sha, Y. Yu, X. Li, H. Hu, and Y. Xing, “Flexible non-sinusoidal zero sequence voltage injection method to extend negative sequence current compensation range for star-connected CHB STATCOM,” *IEEE Trans. Power Electron.*, vol. 36, no. 10, pp. 11357–11371, Oct. 2021.

[33] G. Farivar, C. D. Townsend, B. Hredzak, J. Pou, and V. G. Agelidis, “Passive reactor compensated cascaded H-bridge multilevel LC-StatCom,” *IEEE Trans. Power Electron.*, vol. 32, no. 11, pp. 8338–8348, Nov. 2017.

[34] I. Bourguiba, A. Houari, H. Belloumi, and F. Kourda, “Control of single-phase grid connected photovoltaic inverter,” in *Proc. 4th Int. Conf. Control Eng. Inf. Technol.*, 2016, pp. 1–6.

[35] S. Prakash, J. K. Singh, R. K. Behera, and A. Mondal, “A type-3 modified SOGI-PLL with grid disturbance rejection capability for single-phase grid-tied converters,” *IEEE Trans. Ind. Appl.*, vol. 57, no. 4, pp. 4242–4252, Jul./Aug. 2021.

[36] C. Zhang, S. Føyen, J. A. Suul, and M. Molinas, “Modeling and analysis of SOGI-PLL/FLL-based synchronization units: Stability impacts of different frequency-feedback paths,” *IEEE Trans . Energy Convers.*, vol. 36, no. 3, pp. 2047–2058, Sep. 2021.

[37] M. K. Mishra and V. N. Lal, “Modified proportional resonant current controller with MPPT for three phase single stage grid integrated PV system,” in *Proc. IEEE Appl. Power Electron. Conf. Expo.*, 2020, pp. 3293–3297.

[38] L. Zhang, L. Harnefors, and H.-P. Nee, “Interconnection of two very weak AC systems by VSC-HVDC links using power-synchronization control,” *IEEE Trans. Power Syst.*, vol. 26, no. 1, pp. 344–355, Feb. 2011.

[39] N. Nupur and S. Nath, “Unifying inductor current ripples and inductor design in coupled SIDO converters by forming sectors of duty ratios,” *IEEE Trans. Ind. Appl.*, vol. 58, no. 3, pp. 3830–3839, May/Jun. 2022.

[40] Y. Yuan, J. Zhou, X. Zhao, and G. Xu, “Capacitance design for low-capacitance cascaded H-bridge STATCOM considering inductive demand,” in *Proc. IEEE 4th Int. Elect. Energy Conf.*, 2021, pp. 1–4.